

Final author response – manuscript esurf-2015-43.

Please find below our final response to all referee comments for this manuscript. We first respond to each set of referee comments and explain how we have addressed their concerns in the revised manuscript. A marked-up, revised version of the original manuscript follows our response to the reviewer's comments, and clearly displays where all changes have been made. We hope that the manuscript is now acceptable for publication in *Earth Surface Dynamics*.

Response to comments from anonymous referee #1

Referee comments appear in *italics*. Author response and changes made to the revised manuscript appear in **bold**.

This is really an interesting paper. The authors analysed the inter-annual surface evolution of an Antarctic blue-ice moraine using multi-temporal DEMs. These were obtained from different sources of data and remote sensing techniques: terrestrial lidar and structure-from-motion. The authors considered the three-dimensional "cloud-to-cloud" distance calculations to quantify the moraine surface evolution.

I haven't major issues to provide, the paper is really well written. I have just minor points. The paper, because of the lack of a detailed discussion on processes, it looks like a technical note paper (in the hands of the Editor and Guest Editor the decision on the format of the paper).

We thank the reviewer for their very positive general comments on the manuscript. We have significantly expanded the discussion of glaciological process analysis, which now places our results into their wider glaciological context and with direct reference to existing studies at the Patriot Hills site and further afield (see new line 429 onwards). We believe that the addition of this text ensures that the paper now stands on its own as a full-length research article.

The authors highlighted the fact that "A comprehensive analysis of the evolution of the Patriot Hills blue-ice moraine and its relationships to ablation and underlying ice structure" is not the main purpose of the present work. They just provided few sentences on Earth surface changes interpretation. Why not restructure a little this final section of the discussion highlighting the real addressed value (and application in other contexts) of such inter-annual analysis for understanding the Earth surface processes in a glaciated landscape? How can such analysis be used? For which specific process? Under which environmental forcing?

As suggested, we have restructured and significantly expanded our discussion of the glaciological process analysis at the Patriot Hills study site, which now places our results in the wider context of their real value for understanding inter-annual development of the moraine system (see new line 429 onwards). We now also conclude this new section with a brief discussion of the wider merits of fully 3-D topographic differencing in some other environmental contexts.

Response to comments from anonymous referee #2

General comments:

The paper presents results from two techniques measuring the elevation of a blue ice moraine in very high resolution. The results are interesting, and demonstrate the use of the two techniques in a challenging environment. The results are discussed in a very descriptive way, however, with little analysis and discussion of the results. The discussion of the results

is dismissed slightly off-handedly to another paper. As Reviewer 1 suggests, this is probably a stylistic matter to be flagged up for the Editor.

We thank the reviewer for their positive general comments on the manuscript, and also note the request for an expanded discussion of the results by reviewer #1. To this end, we have substantially expanded our discussion of the results from a glaciological process analysis perspective (see new section 5). Here, we compare the results of our topographic change analysis of blue-ice moraine evolution to previous observations of the Patriot Hills moraine complex (e.g. Fogwill et al., 2012; Vieira et al., 2012), and blue-ice moraines elsewhere.

The paper is well written and clear; however, I have one structural issue with it. The TLS and SfM results are used together straightaway in the presentation of the results in Fig. 3, with no consideration of the potential for error/bias between the two techniques. This was my first question when I saw Fig. 3 – I would like to have this discussed first and a difference figure (TLS vs SfM) presented for the whole dataset. I suggest moving the discussion of the difference on page 1328 to before the presentation of the intra/interseason differences.

As per the reviewer's suggestion, we have moved the discussion of the difference on page 1328 to before the presentation and discussion of the intra-/inter-annual differences. As requested, we have also produced a figure (new Fig. 3) to accompany this discussion and which displays TLS vs. SfM differences as an absolute vertical error (Z_{diff}).

Specific comments:

I found the description of the plots on p1326, line 24 quite difficult to follow. The authors refer to striking similarities, but I found it didn't strike me immediately!

We agree that the description of the 3D differencing plots could do with a little work to improve its clarity. To this end, we have re-written sections of this discussion and hope that it is now easier to follow. All references to 'left', 'right' have been removed and replaced with the appropriate cardinal directions (i.e. north, south, east, west etc). Revision of this text and re-orientation of the plan-view figures should now make interpretation more straightforward.

Figure 1: I found it hard to get my head round this figure, even knowing a little bit about the area, I couldn't orient myself or visualise where the moraine was. Part of this comes from the fact that plots B&C are plotted upside down with respect to plot A. I would suggest putting a broader map of the Patriot Hills with respect to the rest of the Ellsworth Mountains and state clearly in the text that the main plots are oriented differently. Can you not plot B&C the other way up so North is upwards, is there a reason you plot it this way up? This would help with the discussion of Easts and Wests in the main text. If the plots are in a Polar Stereographic projection then is it appropriate to put a North arrow on the plot anyway? If B&C were in the same orientation as A, and A had lines of latitude and longitude, then it is easier to work out which direction is which.

We agree with the reviewer that the different orientations and scales of the various panels which comprise Figure 1 may be difficult to interpret. In line with the referee's suggestions, we have re-organised the figure by doing the following:

- added latitude and longitude grid to panel A (now inset in larger panel A)
- include a new panel (A) which shows the broader geographical context of the Heritage Range area

- re-orientate panels B and C so that north is now at the top of the page
- remove the north arrow in panel A

We note that all plan-view figures have also been rotated to match the orientations of panel B and C in Figure 1 and references to 'left' and 'right' in the interpretation of the results have been removed and replaced with the relevant cardinal directions.

Figure 2. This figure is not referred to in the text as far as I can see?

This is a simple oversight on our part. We have added a reference to this figure at new line 113 in the revised manuscript, following a brief description of the site geomorphology.

Figure 5. Can these lines be plotted in colour? I find it very difficult to tell which is which.

Yes – the lines on this graph now appear in different colours to aid interpretation.

1 **Inter-annual surface evolution of an Antarctic blue-ice moraine**
2 **using multi-temporal DEMs**

3
4 **M. J. Westoby¹, S. A. Dunning², J. Woodward¹, A. S. Hein³, S. M. Marrero³, K. Winter¹**
5 **and D. E. Sugden³**

6
7 [1]{Department of Geography, Engineering and Environment, Northumbria University,
8 Newcastle upon Tyne, UK}

9
10 [2]{School of Geography, Politics and Sociology, Newcastle University, Newcastle upon
11 Tyne, UK}

12
13 [3]{School of GeoSciences, University of Edinburgh, Edinburgh, UK}

14
15 Correspondence to: M. J. Westoby (matt.westoby@northumbria.ac.uk)

16
17 **Abstract**

18
19 Multi-temporal and fine resolution topographic data products are being increasingly
20 used to quantify surface elevation change in glacial environments. In this study, we
21 employ 3D digital elevation model (DEM) differencing to quantify the topographic
22 evolution of a blue-ice moraine complex in front of Patriot Hills, Heritage Range,
23 Antarctica. Terrestrial laser scanning (TLS) was used to acquire multiple topographic
24 datasets of the moraine surface at the beginning and end of the austral summer
25 season in 2012/2013 and during a resurvey field campaign in 2014. A
26 complementary topographic dataset was acquired at the end of season 1 through the
27 application of Structure-from-Motion (SfM) photogrammetry to a set of aerial
28 photographs taken from an unmanned aerial vehicle (UAV). Three-dimensional
29 cloud-to-cloud differencing was undertaken using the Multiscale Model to Model
30 Cloud Comparison (M3C2) algorithm. DEM differencing revealed net uplift and
31 lateral movement of the moraine crests within season 1 (mean uplift ~0.10 m), with
32 lowering of a similar magnitude in some inter-moraine depressions and close to the
33 current ice margin. Our results indicate net uplift across the site between seasons 1
34 and 2 (mean 0.07 m). This research demonstrates that it is possible to detect
35 dynamic surface topographical change across glacial moraines over short (annual to
36 intra-annual) timescales through the acquisition and differencing of fine-resolution
37 topographic datasets. Such data offer new opportunities to understand the process
38 linkages between surface ablation, ice flow, and debris supply within moraine ice.

39 1. Introduction

40
41 Fine-resolution topographic data products are now routinely used for the
42 geomorphometric characterisation of Earth surface landforms (e.g. Passalacqua et
43 al., 2014, 2015; Tarolli, 2014). Recent decades have seen the advent and uptake of
44 a range of surveying technologies for characterising the form and evolution of Earth
45 surface topography at the macro- (landscape; kilometres), meso- (landform; metres)
46 and micro-scales (patch-scale; centimetre-millimetre). These technologies have
47 included, amongst others, the use of satellite remote sensing techniques (e.g. Kääb,
48 2002; Smith et al., 2006; Farr et al., 2007; Stumpf, 2014; Noh and Howat, 2015), as
49 well as field-based surveying platforms such as electronic distance meters (total
50 station; e.g. Keim et al., 1999; Fuller et al., 2003), differential global positioning
51 systems (dGPS; e.g. Brasington et al., 2000; Wheaton et al., 2010), terrestrial laser
52 scanning (TLS; e.g. Rosser et al., 2005; Hodge et al., 2009), airborne light detection
53 and ranging (LiDAR; e.g. Bollmann et al., 2011) and softcopy or digital
54 photogrammetry (e.g. Micheletti et al., 2015).

55
56 More recently, geoscientists are increasingly adopting low-cost Structure-from-
57 Motion with multi-view stereo (SfM-MVS) methods, which employ computer vision
58 and multi-view photogrammetry techniques to recover surface topography using
59 optical (e.g. James and Robson, 2012; Westoby et al., 2012; Javernick et al., 2014;
60 Micheletti et al., 2014; Woodget et al., 2015; Smith and Vericat, 2015) or thermal
61 imagery (e.g. Lewis et al., 2015). Concomitant developments in lightweight
62 unmanned aerial vehicle (UAV) technology, specifically decreasing system costs,
63 increased portability, and improvements in the accessibility of flight planning
64 software have encouraged the acquisition of repeat, fine-resolution (metre to
65 centimetre) topographic data products from low-altitude aerial photography platforms
66 (e.g. Niethammer et al., 2010; Ouédraogo et al., 2014; [Bhardwaj et al., 2016](#)).
67 Furthermore, the differencing of topographic datasets acquired at different times is
68 now an established method for quantifying the transfer of mass and energy through
69 landscapes at the spatial scales of observation at which many processes operate
70 (Passalacqua et al., 2015).

71
72 To date, fine-resolution topographic datasets produced using airborne or ground-
73 based light detection and ranging (LiDAR), or terrestrial or low-altitude aerial digital
74 photogrammetry have been used for a diverse range of applications in various
75 glacial, proglacial, and periglacial environments at a range of scales, including: the
76 quantification of ice surface evolution (e.g. Baltsavias et al., 2001; Pitkänen and
77 Kajuutti, 2004; Keutterling and Thomas, 2006; Schwalbe and Maas, 2009;

78 Immerzeel et al., 2014; Pepin et al., 2014; Whitehead et al., 2014; Gabbud et al.,
79 2015; Kraaijenbrink et al., 2015; Piermattei et al., 2015; Ryan et al., 2015); mapping
80 the redistribution of proglacial sediment (e.g. Milan et al., 2007; Irvine-Fynn et al.,
81 2011; Dunning et al., 2013; Staines et al., 2015) and moraine development
82 (Chandler et al., 2015); the characterisation of glacier surface roughness (e.g. Sanz-
83 Ablanedo et al., 2012; Irvine-Fynn et al., 2014), sedimentology (Westoby et al., [in
84 press2015](#)), and hydrology (Ripplin et al., 2015); as well as input data for surface
85 energy balance modelling (e.g. Arnold et al., 2006; Reid et al., 2012); and for
86 characterising glacial landforms in formerly glaciated landscapes (e.g. Smith et al.,
87 2009; Tonkin et al., 2014; Hardt et al., 2015).

88

89 In this study, we utilise fine-resolution topographic datasets to quantify the surface
90 evolution of a blue-ice moraine complex in a remote part of Antarctica. Blue-ice
91 areas cover approximately 1% of Antarctica's surface area (Bintanja, 1999), yet they
92 remain relatively understudied. Relict blue-ice moraines preserved on nunataks are
93 key indicators of ice sheet elevation changes; however, limited data exist on rates
94 and patterns of surface reorganisation, which may be of use for contextualising the
95 results of, for example, cosmogenic nuclide dating and geomorphological mapping.
96 This research seeks to quantify the short-term surface evolution of a moraine
97 complex in Patriot Hills, Heritage Range, Antarctica (Fig. 1), through the differencing
98 and analysis of multi-temporal topographic datasets acquired using TLS and the
99 application of SfM-MVS photogrammetry to optical imagery acquired from a low-
100 altitude UAV sortie.

101

102 **2. Study site**

103

104 The study site is a blue-ice moraine complex, located on the northern flank of the
105 Patriot Hills massif at the southern-most extent of Heritage Range, West Antarctica
106 (Fig. 1). Blue-ice moraine formation is hypothesised to be the result of preferential
107 ablation of marginal ice by katabatic winds, which in turns prompts the modification
108 of ice flow and englacial sediment transport pathways such that basal sediment is
109 brought to the ice surface, where it is deposited (e.g. Bintanja, 1999; Sinisalo and
110 Moore, 2010; Fogwill et al., 2012; Spaulding et al., 2012; [Hein et al., 2016](#)). The site
111 comprises a series of broadly east-west oriented moraine ridges and inter-moraine
112 troughs, as well as an area of subdued moraine topography immediately adjacent to
113 the ice margin ([Fig. 2](#)). At this location, the active blue-ice moraines occupy an
114 altitudinal range of 60-70 m above the ice margin (~730 m a.s.l.), and extend for a
115 distance of up to 350 m into a bedrock embayment. The blue-ice moraines can be
116 traced for a distance of >4 km to the east and north-east, parallel to the range front,

117 and fill ice-marginal embayments. The site is geomorphologically and
118 sedimentologically complex (e.g. Vieira et al., 2012; Westoby et al., [in press 2015](#)),
119 and, along with moraine ridges and troughs, includes areas of subdued ice-marginal
120 topography with thermokarst melt ponds, local gullying and crevassing on ice-
121 proximal and distal moraine flanks, as well as solifluction deposits at the base of the
122 surrounding hillslopes. The bedrock hillslopes are overlain by a till drape with rare,
123 large exotic sandstone boulder erratics which have some evidence of periglacial
124 reworking. Field observations suggest that the blue-ice moraines are dynamic
125 features which are undergoing localised surface changes. It is these short-term,
126 changes which are the subject of investigation in this paper.

127

128 **3. Methods and data products**

129

130 This research employs two methods for reconstructing moraine surface topography,
131 specifically TLS and SfM-MVS photogrammetry. Two field campaigns at Patriot Hills
132 were undertaken with a 12-month survey interval. Briefly, TLS data were acquired at
133 the beginning and end of austral summer season 1 (December 2012 and January
134 2013, respectively), and in a short resurvey visit in season 2 (January 2014). Low-
135 altitude aerial optical photography was acquired from a UAV at the end of season 1
136 and was used as the primary input to SfM-MVS processing. The following sections
137 detail the two methods of topographic data acquisition, data processing, and
138 subsequent analysis using 'cloud-to-cloud' differencing.

139

140 **3.1. Topographic data acquisition**

141

142 **3.1.1. Terrestrial Laser Scanning**

143

144 TLS data were acquired using a Riegl LMS-Z620 time-of-flight laser scanner, set to
145 acquire ~11,000 points per second in the near-infrared band at horizontal and
146 vertical scanning increments of 0.031°, equivalent to a point spacing of 0.05 m at a
147 distance of 100 m and with a beam divergence of 15 mm per 100 m. Data were
148 acquired from six locations across the site at the beginning of season 1 (7th-11th
149 December 2012; Fig. 1; Table 1). Two of these positions were re-occupied at the
150 end of season 1 (9th January 2013) and three positions were reoccupied in season 2
151 (Fig. 1; 14th January 2014). Following manual editing and the automated removal of
152 isolated points to improve data quality, each set of scans were co-registered in Riegl
153 RiSCAN PRO software (v. 1.5.9) using a two-step procedure employing coarse
154 manual point-matching followed by the application of a linear, iterative, least-squares
155 minimisation solution to reduce residual alignment error. Individual scans were then

156 merged to produce a single 3D point cloud for each scan date. Merged scan data
157 from the end of seasons 1 and 2 were subsequently registered to the scan data from
158 the beginning of season 1 using the methods described above (Table 1).

159

160 **3.1.2. Structure-from-Motion with Multi-View Stereo photogrammetry**

161

162 Low-altitude aerial photographs of the study site were acquired using a 10-Megapixel
163 Panasonic Lumix DMC-LX5 compact digital camera with a fixed focal length (8 mm)
164 and automatic exposure settings, mounted in a fixed, downward-facing (nadir)
165 perspective on a sub-5 kg fixed-wing UAV. Photographs were acquired in a single
166 sortie lasting ~5 minutes. A total of 155 photographs were acquired at a 2-second
167 interval at an approximate ground height of 120 m, producing an average image
168 overlap of 80%, and an approximate ground resolution of 0.07 m² per pixel. Mean
169 point density was ~300 points per m², compared to a mean of 278 points per m² for
170 the TLS datasets. Motion blur of the input images was negligible due to favourable
171 image exposure conditions and an appropriate UAV flying height and speed.

172

173 UAV photographs were used as input to SfM reconstruction using the proprietary
174 Agisoft PhotoScan Professional Edition (v. 1.1.6) software. Unique image tie-points
175 which are stable under variations in view perspective and lighting are identified and
176 matched across input photographs, similar to Lowe's (2004) Scale Invariant Feature
177 Transform (SIFT) method. An iterative bundle adjustment algorithm is used to solve
178 for internal and external camera orientation parameters and produce a sparse 3D
179 point cloud. The results of the first-pass camera pose estimation were scrutinised
180 and only 3D points which appear in a minimum of 3 photographs and possessed a
181 reprojection error of <1.0 were retained. A two-phase method of UAV-SfM data
182 registration was employed: 1) ground control was obtained by identifying common
183 features in the UAV-SfM photographs and TLS data from the end of season 1
184 (acquired 4 days after the SfM data; Table 1), such as the corners of large, well-
185 resolved boulders. GCP data were used to optimise the initial camera alignment and
186 transform the regenerated UAV-SfM data to the same object space as the TLS data,
187 producing an xyz RMS error of 0.23 m. 2) following dense reconstruction, 3D point
188 data were exported to RiSCAN PRO (v. 1.5.9) software, and a linear, iterative, least-
189 squares minimisation employing surface plane matching was used to improve the
190 alignment and reduce the xyz RMS error to 0.03 m.

191

192 **3.2. Cloud-to-cloud differencing**

193

194 Three-dimensional ‘cloud-to-cloud’ distance calculations were used to quantify
195 moraine surface evolution (e.g. Lague et al., 2013). Since the dominant direction of
196 surface evolution across the study site was unknown *a priori*, the application of an
197 algorithm that is capable of detecting fully three-dimensional topographic change
198 was deemed to be the most appropriate method in this context. To this end, we
199 employ the Multiscale Model to Model Cloud Comparison (M3C2) algorithm (Lague
200 et al., 2013; Barnhart and Crosby, 2013), implemented in the open-source
201 CloudCompare software (v. 2.6.1) for change detection.

202
203 The M3C2 algorithm implements two main processing steps to calculate 3D change
204 between two point clouds: 1) estimation of surface normal orientation at a scale
205 consistent with local surface roughness, and 2) quantification of the mean cloud-to-
206 cloud distance (i.e. surface change) along the normal direction (or orthogonal
207 vector), which includes an explicit calculation of the local confidence interval. A point-
208 specific normal vector is calculated by fitting a plane to neighbouring 3D points that
209 are contained within a user-specified search radius. To avoid the fluctuation of
210 normal vector orientations and a potential overestimation of the distance between
211 two point clouds, the radius, or scale, used for normal calculation needs to be larger
212 than the topographic roughness, which is calculated as the standard deviation of
213 local surface elevations (σ). The orientation of the surface normal around a point, i , is
214 therefore dependent on the scale at which it is computed (Lague et al., 2013). A trial-
215 and-error approach was employed to reduce the estimated normal error, $E_{\text{norm}}(\%)$,
216 through refinement of a re-scaled measure of D , ξ , where:

217
218
$$\xi(i) = \frac{D}{\sigma_i(D)} \quad \text{Eq. (1)}$$

219
220 Using this re-scaled measure of D , ξ can be used as an indicator of estimated normal
221 orientation accuracy, such that where ξ falls in the range ~20-25, the estimated
222 normal error is $E_{\text{norm}} < 2\%$ (Lague et al., 2013). A fixed normal scaling of 2 m was
223 found to be sufficient to ensure that $\xi > 20$ for >98% of points in each topographic
224 dataset.

225
226 The radius of the projection cylinder, d , within which the average surface elevation of
227 each cloud is calculated, was specified as 2 m. This scaling ensured that the number
228 of points sampled in each cloud was ≥ 30 , following guidance provided by Lague et
229 al. (2013). M3C2 execution took ~0.3 h for each differencing task on a desktop
230 computer operating with 32 GB of RAM, and a 3.4 GHz CPU. Cloud-to-cloud
231 distances and statistics were projected onto the original point cloud. M3C2 output

232 was subsequently masked to exclude points where change is lower than level of
233 detection threshold for a 95% confidence level, $LoD_{95\%}(d)$, which is defined as:

$$235 \quad LoD_{95\%}(d) = \pm 1.96 \left(\frac{\sigma_1(d)^2}{n_1} + \frac{\sigma_2(d)^2}{n_2} + reg \right) \quad \text{Eq. (2)}$$

236
237 where d is the radius of the projection cylinder, reg is the user-specified registration
238 error, for which we substitute the propagated root mean square alignment error for
239 point clouds n_1 and n_2 (Table 2; Eq. (1)) and assume that this error is isotropic and
240 spatially uniform across the dataset.

241
242 To calculate the total propagated error for each differencing epoch, σ_{DoD} , the
243 estimates of errors in each point cloud (i.e. the sum of the average scan-scan RMS
244 error and a project-project RMS error, where applicable) were combined using:

$$246 \quad \sigma_{DoD} = \sqrt{\sigma_{C_1}^2 + \sigma_{C_2}^2} \quad \text{Eq. (3)}$$

247
248 where $\sigma_{C_1}^2$ and $\sigma_{C_2}^2$ are the RMS errors associated with point clouds C_1 and C_2 .

249 **3.3. Data intercomparison: SfM vs. TLS**

Formatted: Font: Bold

Formatted: Font: Bold

250
251 Whilst the UAV-SfM dataset acquired at the end of season 1 significantly improves
252 on the spatial coverage afforded by the use of TLS across the moraine embayment,
253 an analyses of the relative accuracy of the reconstructed surface topography of the
254 former is desirable. To this end, Fig. 3 shows the results of vertical differencing of the
255 UAV-SfM and TLS data, complemented by a series of surface elevation profiles (Fig.
256 4). These results reveal that 83% of the UAV-SfM data are within ± 0.1 m of the
257 equivalent TLS data, with a number of outliers at the northernmost margin of the
258 dataset, where the UAV-SfM data typically underestimate the TLS surface elevation.
259 Similarly, the UAV-SfM data underestimate the surface elevation of the ice-proximal
260 flank of the main moraine crest by, on average, ~ 0.13 m. UAV-SfM data
261 overestimate the moraine surface elevation in the north-western sector of the site by
262 ~ 0.12 m, with some outliers which exceed ~ 0.3 m.

Formatted: Font color: Auto

Formatted: Font color: Auto

263
264
265
266 Transect data also highlight areas of inconsistency, specifically often considerable
267 offsets between the TLS and SfM data which were collected at the end of season 1
268 and which, in places, approach 0.5 m in magnitude (e.g. at ~ 27 m distance in profile
269 A, and between 22-30 m in profile B; Fig. 4). Given that the SfM data were optimised

270 and georegistered using features extracted from the corresponding TLS dataset, one
271 might expect that deviations between the two would be barely discernible. However,
272 the SfM data variously over- and underestimate the TLS-derived surface elevation
273 with little apparent systematicity (Fig. 4). One potential explanation for these
274 inconsistencies could be the evolution of moraine surface topography in the 4-day
275 interval which separated the acquisition of the TLS and SfM data at the end of
276 season 1 (Table 1), with the implication that features used as GCPs in the TLS data
277 and their counterparts in the UAV-SfM data were not static, thereby affecting the
278 georeferencing and SfM optimisation solution. However, as we observe no clustering
279 of large GCP errors in areas of activity, this factor is unlikely to account for these
280 topographic inconsistencies.

281
282 An additional, and equally viable explanation for these inconsistencies might include
283 the near-parallel and largely nadir view directions of the UAV imagery, which
284 represent a largely 'non-convergent' mode of photograph acquisition that has
285 elsewhere been found to result in the deformation, or 'doming' of SfM-derived
286 surface topography (e.g. James and Robson, 2014; Rosnell and Honkavaara, 2012;
287 Javernick et al., 2014). Topographic mismatches between the TLS and UAV-SfM
288 data appear to be the most prominent in areas of steep topography (Fig. 3; Fig. 4).
289 These areas were generally well-resolved in the TLS data (where not topographically
290 occluded), but may have been resolved in less detail and with less accuracy in the
291 UAV-SfM data, where the fixed camera angle promotes the foreshortening of these
292 steep slopes in the aerial photography. Model deformations can be countered to
293 some degree through the inclusion of additional, oblique imagery, and use of suitable
294 GCPs (James and Robson, 2014). However, although the latter were relatively
295 evenly spaced across our study site, the inclusion of these data and subsequent use
296 for the optimisation of the SfM data prior to dense point cloud reconstruction does
297 not appear to have altogether eliminated these model deformations.

Formatted: Font color: Auto

298

299

300

4. Short-term topographic evolution of blue-ice moraines

301

302

The results of 3D cloud-to-cloud differencing are summarised in Figures ~~35 to 5~~.
303 Threshold levels of change detection ranged from 0.094 – 0.103 m. The upper (i.e.
304 most conservative) bound of this range was applied to the results from all
305 differencing epochs, so that only 3D surface changes greater than 0.103 m were
306 considered in the subsequent analysis. The horizontal (xy) and vertical (z)
307 components of 3D surface change were separated to aid the analysis and
308 interpretation of moraine surface evolution. Vertical surface changes for a range of
309 epochs, encompassing intra-annual and annual change, are displayed in Fig. 53,

310 | whilst ~~the illustrative~~ horizontal components of 3D change are shown in Fig. 46. The
311 | longest differencing epoch, representing a period of ~400 days (Fig. 53b) shows a
312 | broad pattern of net uplift across the moraine of the order of 0.074 m. Locally, uplift
313 | exceeds 0.2 m across parts of the moraine complex, and, whilst on first glance these
314 | elevation gains appear to be largely randomly distributed across the site, on closer
315 | inspection they occur predominantly on or adjacent to the main, central moraine
316 | ridge and close to the current ice margin. The large central moraine ridge exhibits a
317 | mean uplift of 0.11 m, whilst specific ice-marginal areas to the ~~bottom-right (west),~~
318 | and an area of moraine ~~to the in the top-right (south-west)~~ of the embayment also
319 | exhibit uplift of a similar magnitude (Fig. 35b). In contrast, an area ~~at the centre-top~~
320 | ~~in the (southernmost) extent sector~~ of the basin and an ice-marginal area to the
321 | centre-west exhibit a net reduction in moraine surface elevation, up to a maximum of
322 | -0.354 m.

323 |
324 | Intra-annual change detection mapping was undertaken using TLS-TLS and TLS-
325 | SfM differencing (Fig. 53c, d). Key similarities between these two datasets, which
326 | represent vertical topographic change over a ~31 and ~27 day period, respectively,
327 | include uplift at the ~~centre-left (south-eastern) southern~~ extent of the embayment
328 | (mean 0.081 m and 0.123 m for the TLS-TLS and TLS-SfM differencing,
329 | respectively). Similarly, both datasets reveal surface lowering ~~at south-eastern, or~~
330 | ~~true rear, of the basin to the centre-rear of the site~~ (mean -0.106 m and -0.112 m for
331 | TLS-SfM and TLS-TLS differencing, respectively), and, in the TLS-SfM data, on the
332 | ice-distal (southern) side of the central moraine ridge (Fig. 35c; -0.092 m). However,
333 | the large area of ice-marginal surface lowering (-0.095 - -0.373 m) that is detected in
334 | the TLS-SfM differencing results is not mirrored in the equivalent TLS-TLS
335 | differencing data (Fig. 35d). This stems in large part from the reduced spatial
336 | coverage of the usable TLS scan data acquired at the end of season 1, which
337 | comprised data from only two scan positions (Fig. 1c) and which omits the ice-
338 | marginal zone.

339 |
340 | The results of vertical change detection using both SfM-TLS and TLS-TLS
341 | approaches also display ~~striking~~ similarities for differencing undertaken between the
342 | end of season 1, and season 2 (Fig. 35e,f), including a largely continuous area of
343 | uplift across the ~~central portion~~ centre of the site, as well as areas of surface lowering
344 | ~~along to the eastern centre-left (eastern) extent edge~~ of the site. Whilst widespread
345 | uplift characterises the entire western ~~(right)~~ edge of the study area in the TLS-TLS
346 | data (Fig. 53f), the equivalent SfM-TLS data instead report the occurrence of surface
347 | lowering at the base of the hillslope spur which forms the western boundary of the
348 | site (Fig. 35e). Furthermore, an area of considerable (mean 0.218 m) uplift

349 characterises the ice-marginal zone in the SfM-TLS differencing data for this epoch,
350 but, once again, the reduced spatial coverage of the TLS datasets mean that no
351 differencing data are available to verify or contest this pattern. However, we note that
352 vertical change at the ice-marginal (northern) limit of the TLS-TLS data for both intra-
353 annual and annual differencing epochs do not correspond with the equivalent SfM-
354 TLS / TLS-SfM results.

355
356 Examples of horizontal displacement, calculated here as the xy component of the
357 orthogonal distance between two point clouds acquired at separate times, and
358 gridded to represent the average xy displacement within 10 m^2 grid cells, are shown
359 in Fig. 46 for intra- (Fig. 46a) and inter-annual epochs (Fig. 64b). Within season 1, a
360 range of xy displacement orientations are detected, and range from sub-centimetre
361 to $>0.2\text{ m}$ in magnitude. These displacements include extensive southern (or
362 'inward') movement of the moraine surface in the ice-marginal zone, which is
363 associated with surface lowering, and which grades into a largely western-oriented
364 displacement signal on the ridgeline of the main moraine crest and across the
365 ~~centre-right~~ (western) sector of the moraine complex (Fig. 4a6a). Total xy
366 displacement over a >1 year period (Fig. 4b6b) appears to be less uniform and
367 comparatively chaotic. However, a number of local and largely consistent patterns of
368 horizontal displacement are discernible, such as predominantly westward movement
369 along the central moraine ridge, and north- to north-eastern motion along the
370 western edge of the site (Fig. 46b), which also occurs within season 1 (Fig. 64ea).
371 Both trends are associated with net surface uplift. In contrast, isolated patches of
372 surface lowering are generally characterised by southern or south-westerly xy
373 displacement.

374
375 The analysis of a series of surface profile transects which bisect the moraines shed
376 further light on their topographic evolution (Fig. 54). These data are particularly
377 useful for examining the interplay between vertical and lateral moraine surface
378 displacement, which is alluded to in Fig. 46. For example, a combination of surface
379 uplift and lateral displacement between the start and end of season 1 is visible
380 between 28-40 m in profile A (Fig. 54, inset 1). Similarly, lateral (southern) translation
381 of the moraine surface between 15-22 m in profile C (Fig. 54, inset 2) is visible for
382 the same differencing epoch.

383
384 ~~These transect data also highlight areas of inconsistency, specifically often~~
385 ~~considerable offsets between the TLS and SfM data which were collected at the end~~
386 ~~of season 1 and which, in places, approach 0.5 m in magnitude (e.g. at 27 m~~
387 ~~distance in profile A, and between 22-30 m in profile B; Fig. 5). Given that the SfM~~

388 data were optimised and georegistered using features extracted from the
389 corresponding TLS dataset, one might expect that deviations between the two would
390 be barely discernible. However, the SfM data variously over- and underestimate the
391 TLS-derived surface elevation with little apparent systematicity (Fig. 5). One potential
392 explanation for these inconsistencies could be the evolution of moraine surface
393 topography in the 4-day interval which separated the acquisition of the TLS and SfM
394 data at the end of season 1 (Table 1), with the implication that features used as
395 GCPs in the TLS data and their counterparts in the UAV-SfM data were not static,
396 thereby affecting the georeferencing and SfM optimisation solution. However, as we
397 observe no clustering of large GCP errors in areas of activity, this factor is unlikely to
398 account for these topographic inconsistencies.

399 An additional, and equally viable explanation for these inconsistencies might include
400 the near-parallel and largely nadir view directions of the UAV imagery, which
401 represent a largely 'non-convergent' mode of photograph acquisition that has
402 elsewhere been found to result in the deformation, or 'doming' of SfM-derived
403 surface topography (e.g. James and Robson, 2014; Rosnell and Honkavaara, 2012;
404 Javernick et al., 2014). Topographic mismatches between the TLS and UAV-SfM
405 data appear to be the most prominent in areas of steep topography (Fig. 5). These
406 areas were generally well-resolved in the TLS data (where not topographically
407 occluded), but may have been resolved in less detail and with less accuracy in the
408 UAV-SfM data, where the fixed camera angle promotes the foreshortening of these
409 steep slopes in the aerial photography. Model deformations can be countered to
410 some degree through the inclusion of additional, oblique imagery, and use of suitable
411 GCPs (James and Robson, 2014). However, although the latter were relatively
412 evenly spaced across our study site, the inclusion of these data and subsequent use
413 for the optimisation of the SfM data prior to dense point cloud reconstruction does
414 not appear to have altogether eliminated these model deformations (Fig. 5).

415
416
417 The above shortcomings notwithstanding, this research nevertheless represents the
418 first successful application of a combination of high-resolution surveying methods for
419 quantifying the topographic evolution of ice-marginal topography in this environment.
420 This study has demonstrated that, whilst a number of operational considerations,
421 such as the requirement for multiple TLS station positions to acquire satisfactory
422 spatial coverage across a topographically complex site of this size, and the
423 necessary deployment of an independent set of dedicated GCPs for accurate UAV-
424 SfM georegistration or the acquisition of additional, oblique aerial photographs, must
425 be taken into account, these technologies are appropriate for reconstructing blue-ice

426 ~~moraine surface topography. Furthermore, the use of fully 3D differencing algorithms~~
427 ~~is appropriate for quantifying inter-annual to annual moraine surface evolution.~~

428

429 **5. Implications for glaciological process analysis**

430

431 ~~A comprehensive analysis of the evolution of the Patriot Hills blue-ice moraine and~~
432 ~~its relationships to ablation and underlying ice structure is the focus of another study,~~
433 ~~but Here we it is worth highlighting~~ some implications arising from the measurement
434 of these short-term changes in surface morphology. Topographically, the Patriot Hills
435 blue-ice moraine confirms the morphological observations of the embayment,
436 described by Fogwill et al. (2012) as comprising sloping terraces and blocky, pitted
437 boulder moraine ridges. These ridges are thought to be fed from beneath by steeply
438 dipping debris bands coming from depth, driven by ice-flow compensating for
439 katabatic wind ablation of the glacier. Vieira et al. (2012) classify what we term blue-
440 ice moraines as ‘supraglacial moraine’, and the debris bands in the blue ice outside
441 of the basin as blue-ice moraines. It is from clasts emerging from these bands that
442 Fogwill et al. (2012) have produced their model of blue-ice moraine formation in the
443 basin. The supraglacial moraines of Vieira et al. (2012) are described as slightly
444 creeping debris-mantled slopes – both Fogwill et al. (2012) and Vieira et al. (2012)
445 consider the features in the basin as active, but without measurements of
446 observations of rates, or the nature of change. Our differencing results confirm the
447 hypothesis that these features are active, and develops this idea further to
448 demonstrate that moraine slope evolution is active over annual to intra-annual
449 timescales.

450

451 Hättestrand and Johansen (2005) discussed the evolution of blue-ice moraine
452 complexes in Dronning Maud Land, Antarctica, and hypothesised that, following ice-
453 marginal deposition of debris when the adjacent ice surface was higher, the
454 subsequent lowering of the exposed ice surface would produce a slope ‘outwards’
455 from an embayment, followed by gradual movement of material towards the ice-
456 margin in a manner similar to that exhibited by active rock glaciers – features that
457 Vieira et al. (2012) interpret in the next basin along the Patriot Hills range. However,
458 whilst the former holds true as an explanation for the general gradient of the Patriot
459 Hills moraine complex (e.g. Fig. 4), our results suggest that the short-term evolution
460 of the moraines does not necessarily conform to the latter hypothesis of such as
461 simple process of consistent downslope movement, and in fact exhibits far more
462 dynamic complexity.

463

464 ~~Firstly, t~~The moraine ridges both close to, and far from the ice margin emerge as

Formatted: Line spacing: Multiple 1.3 li

Formatted: Font: Bold

Formatted: Font: 12 pt, Bold

Formatted: List Paragraph, Indent: Left: 0 cm, Hanging: 0.5 cm, Outline numbered + Level: 1 + Numbering Style: 1, 2, 3, ... + Start at: 1 + Alignment: Left + Aligned at: 0.63 cm + Indent at: 1.27 cm

Formatted: Left

Formatted: Font color: Background 1

465 axes of activity and uplift (Fig. 53c), despite initial field observations suggesting that
466 the ridges most distant from the exposed ice surface were older and less active.-
467 Fogwill et al. (2012) suggest that once upcoming debris is at a sufficient thickness,
468 wind-driven ablation shuts off. Our observations suggest that if this is the case, these
469 ridges are not left stagnant at this point. The interplay between ice flow and surface
470 elevation lowering by wind, but reduced by thicker debris, continues despite the
471 possible ages of the surface debris relative to ridges closer to the contemporary
472 blue-ice margin. This activity is not simply confined to 'inward' or 'outward'
473 movement of moraines within the embayment, but also involves a lateral component.
474 Secondly, the surface lowering is the result of ablation and it is notable that most
475 lowering occurred near the ice margin where the debris layer is typically thinnest and
476 less than ~0.15 m. Surface lowering in this area exceeds 0.3 m within season 1 (Fig.
477 5c), and may be the result of sub-debris ice ablation, which promotes terrain
478 relaxation and has been widely reported in other ice-proximal landscapes (e.g.
479 Krüger and Kjær, 2000; Schomacker, 2008; Irvine-Fynn et al., 2011; Staines et al.,
480 2015).

481
482 Lateral movement within the moraine ridges (Fig. 6) may reflect lateral extension or
483 'stretching' of the ridges as they encroach into the embayment. Such lateral
484 movement is corroborated from the orientation of crevasse-based grooves in the
485 moraine (Fig. 2c). The apparent inward encroachment of the Patriot Hills moraines
486 may be the product of the pressure exerted on the moraines by glacier ice flow into
487 the embayment in compensation for preferential ice ablation by katabatic winds,
488 which is consistent with blue-ice moraine formation theory (Fogwill et al., 2012).
489 Finally, the close match of inter-season surface elevation cross-profiles between
490 seasons (Fig. 5) points to medium-term stability of the moraine system. This
491 conclusion will be investigated through the application of cosmogenic isotope
492 evidence to assess change since the Holocene.

493
494 More broadly, this study has demonstrated the potential for the combination of
495 different high-resolution surveying technologies and advanced, 3D topographic
496 differencing methods for elucidating the short-term evolution of glaciated landscapes.
497 Whilst this study has focused exclusively on the surface evolution of Antarctic blue-
498 ice moraines, the application of 3D differencing methods to quantify change between
499 repeat, accurate topographic surveys has a wide range of potential glaciological
500 applications, which cryospheric researchers have already begun to capitalise on
501 (e.g. Piermattei et al., 2015, Gabbud et al., 2015; Kraaijenbrink et al., 2016). A key
502 contribution of this study to the wider Earth surface dynamics community is the
503 demonstration of truly 3D differencing methods to reveal not only vertical surface

Formatted: Font: 12 pt

Formatted: Normal, Left, Line
spacing: Multiple 1.3 li, No bullets or
numbering

Formatted: Font: 12 pt

Formatted: Font: 12 pt

Formatted: Font: 12 pt

504 change, but also the magnitude and direction of any lateral component to surface
505 movement. Such methods may have particular value for quantifying the 3D surface
506 evolution of, for example, rock glaciers, degrading ice-cored moraines, or slope
507 instabilities in permafrost regions, where information regarding both vertical and
508 lateral components of landscape development may be both of scientific interest and
509 practical application.

Formatted: Font: 12 pt

Formatted: Font: 12 pt

Formatted: Font: 12 pt

510
511 6.

Formatted: Font: 12 pt

Formatted: Left

Formatted: Font: Bold

Formatted: Font: 12 pt

Formatted: Left, Line spacing:
Multiple 1.3 li

Formatted: Normal, Left, Line
spacing: Multiple 1.3 li, No bullets or
numbering

512 **5. Summary**

514 This research has employed a combination of TLS and UAV-based SfM-MVS
515 photogrammetry and 3D differencing methods to quantify the topographic evolution
516 of an Antarctic blue-ice moraine complex over annual and intra-annual timescales.
517 Segmentation of lateral and vertical surface displacements reveal site- and local-
518 scale patterns of geomorphometric moraine surface evolution beyond a threshold
519 level of detection (95% confidence), including largely persistent vertical uplift across
520 key moraine ridges, both within a single season, and between seasons. This
521 persistent uplift is interspersed with areas (and periods) of surface downwasting
522 which is largely confined to the rear of the moraine basin for both differencing
523 epochs, and in ice-marginal regions within season 1. Analysis of lateral displacement
524 vectors, which are generally of a much smaller magnitude than vertical
525 displacements, provide further insights into moraine surface evolution.
526

527
528 A number of methodological shortcomings are highlighted. Briefly, these relate to the
529 incomplete spatial coverage afforded by the use of TLS in a topographically complex
530 environment, and issues associated with obtaining suitable ground control for SfM-
531 MVS processing and potential implications for the accuracy of SfM-derived
532 topographic data products. ~~The research represents the first successful application~~
533 ~~of these techniques in such a remote environment. This research represents the first~~
534 successful application of a combination of high-resolution surveying methods for
535 quantifying the topographic evolution of ice-marginal topography in this environment.
536 Furthermore, we have demonstrated that, whilst a number of operational
537 considerations must be taken into account at the data collection stage, these
538 technologies are highly appropriate for reconstructing moraine surface topography
539 and for quantifying Earth surface evolution in glaciated landscapes more generally.

540
541
542

543 **Author contribution**

544

545 S. A. Dunning, J. Woodward, A. Hein, K. Winter, S. M. Marrero and D. E. Sugden
546 collected field data. TLS and SfM data processing and differencing were undertaken
547 by M. J. Westoby. Data analysis was performed by M. J. Westoby, S. A. Dunning
548 and J. Woodward. Manuscript figures were produced by M. J. Westoby. All authors
549 contributed to the writing and revision of the manuscript.

550

551 **Acknowledgements**

552

553 The research was funded by the UK Natural Environment Research Council
554 (Research Grants NE/I027576/1, NE/I025840/1, NE/I024194/1, NE/I025263/1). We
555 thank the British Antarctic Survey for logistical support.

556 **References**

- 557
558 Agisoft: Agisoft PhotoScan Professional Edition v.1.1.6. Available:
559 <http://www.agisoft.com>, 2014.
560
561 Arnold, N. S., Rees, W. G., Hodson, A. J., and Kohler, J.: Topographic controls on
562 the surface energy balance of a high Arctic valley glacier. *Journal of Geophysical*
563 *Research*, 111, F02011, doi: 10.1029/2005JF000426, 2006.
564
565 Baltsavias, E. P., Favey, E., Bauder, A., Bösch, H., and Pateraki, M.: Digital surface
566 modelling by airborne laser scanning and digital photogrammetry for glacier
567 monitoring. *Photogrammetric Record*, 17, 243-273, doi: 10.1111/0031-868X.00182,
568 2001
569
570 Barnhart, T. B. and Crosby, B. T.: Comparing two methods of surface change
571 detection on an evolving thermokarst using high-temporal-frequency terrestrial laser
572 scanning, Selawik River, Alaska. *Remote Sensing*, 5, 2813-2837, doi:
573 10.3390/rs5062813, 2013.
574
575 [Bhardwaj, A., Sam, L., Akanksha, Martín-Torres, F.J., and Kumar, R.: UAVs as](#)
576 [remote sensing platform in glaciology: Present applications and future prospects.](#)
577 [Remote Sensing of Environment](#), 175, 196-204, doi: 10.1016/j.rse.2015.12.029,
578 [2016.](#)
579
580 Bintanja, R.: On the glaciological, meteorological, and climatological significance of
581 Antarctic blue ice areas. *Reviews of Geophysics*, 37, 337-359, doi:
582 10.1029/1999RG900007, 1999.
583
584 Bollmann, E., Sailer, R., Briese, C., Stotter, J., and Fritzmann, P.: Potential of
585 airborne laser scanning for geomorphologic feature and process detection and
586 quantifications in high alpine mountains. *Zeitschrift für Geomorphologie*, 55, 83-104,
587 doi: 10.1127/0372-8854/2011/0055S2-0047, 2011.
588
589 Brasington, J., Rumsby, B. T., and McVey, R. A.: Monitoring and modelling
590 morphological change in a braided gravel-bed river using high resolution GPS-based
591 survey. *Earth Surface Processes and Landforms*, 25, 973-990, doi: 10.1002/1096-
592 9837(200008)25:9<973::AID-ESP111>3.0.CO;2-Y, 2000.
593
594 Chandler, B. M. P., Evans, D. J. A., Roberts, D. H., Ewertowski, M., and Clayton, A.
595 I.: Glacial geomorphology of the Skálafellsjökull foreland, Iceland: A case study of
596 'annual' moraines. *Journal of Maps*, doi: 10.1080/17445647.2015.1096216, 2015.
597
598 Dunning, S. A., Large, A. R. G., Russell, A. J., Roberts, M. J., Duller, R., Woodward,
599 J., Mériaux, A-S., Tweed, F. S., and Lim, M.: The role of multiple glacier outburst
600 floods in proglacial landscape evolution: The 2010 Eyjafjallajökull eruption, Iceland.
601 *Geology*, 796 41(10), 1123-1136, doi: 10.1130/G34665, 2013.
602
603 Farr, T. G., Rosen, P. A., Caro, E., Crippen, R., Duren, R., Hensley, S., Kobrick, M.,
604 Paller, M., Rodriguez, E., Roth, L., Seal, D., Shaffer, S., Shimada, J., Umland, J.,
605 Werner, M., Oskin, M., Burbank, D., and Alsdorf, D.: The shuttle radar topography

606 mission. *Reviews of Geophysics*, 45(2), RG2004, doi: 10.1029/2005RG000183,
607 2007.

608

609 Fogwill, C. J., Hein, A. S., Bentley, M. J., and Sugden, D. E.: Do blue-ice moraines in
610 the Heritage Range show the West Antarctic ice sheet survived the last interglacial?
611 *Palaeogeography, Palaeoclimatology, Palaeoecology*, 335-336, 61-70, doi:
612 10.1016/j.palaeo.2011.01.027, 2012.

613

614 Fuller, I. C., Large, A. R. G., and Milan, D.: Quantifying channel development and
615 sediment transfer following chute cutoff in a wandering gravel-bed river.
616 *Geomorphology*, 54, 307-323, doi: 10.1016/S0169-555X(02)00374-4, 2003.

617

618 Gabbud, C., Micheletti, N., and Lane, S. N.: Lidar measurement of surface melt for a
619 temperate Alpine glacier at the seasonal and hourly scales. *Journal of Glaciology*,
620 61(229), 963-974, doi: 10.3189/2015JoG14J226, 2015.

621

622 Hardt, J., Hebenstreit, R., Lüthgens, C., and Böse, M.: High-resolution mapping of
623 ice-marginal landforms in the Barnim region, northeast Germany. *Geomorphology*,
624 250, 41-52, doi: 10.1016/j.geomorph.2015.07.045, 2015.

625

626 [Hättestrand, C., and Johansen, N.: Supraglacial moraines in Scharffenbergbotnen,
627 Heimafrontfjella, Dronning Maud Land, Antarctica – significance for reconstructing
628 former blue ice areas. *Antarctic Science*, 17\(2\), 225-236, doi:
629 10.1017/S0954102005002634, 2005.](#)

630

631 [Hein, A.S., Woodward, J., Marrero, S.M., Dunning, S.A., Steig, E.J., Freeman,
632 S.P.H.T., Stuart, F.M., Winter, K., Westoby, M.J., and Sugden, D.E.: Evidence for
633 the stability of the West Antarctic Ice Sheet divide for 1.4 million years. *Nature
634 Communications*, 7, 10325, doi: 10/1038/ncomms10325, 2016.](#)

635

636 Hodge, R., Brasington, J., and Richards, K.: In-situ characterisation of grain-scale
637 fluvial morphology using Terrestrial Laser Scanning. *Earth Surface Processes and
638 Landforms*, 34, 954-968, doi: 10.1002/esp.1780, 2009.

639

640 Immerzeel, W. W., Kraaijenbrink, P. D. A., Shea, J. M., Shrestha, A. B., Pellicciotti,
641 F., Bierkens, M. F. P., and de Jong, S. M.: High-resolution monitoring of Himalayan
642 glacier dynamics using unmanned aerial vehicles. *Remote Sensing of Environment*,
643 150, 93-103, doi: 10.1016/j.rse.2014.04.025, 2014.

644

645 Irvine-Fynn, T. D. L., Sanz-Ablanedo, E., Rutter, N., Smith, M. W., and Chandler, J.
646 H.: Measuring glacier surface roughness using plot-scale, close-range digital
647 photogrammetry. *Journal of Glaciology*, 60(223), 957-969, doi:
648 10.3189/2014JoG14J032, 2014.

649

650 James, M. R., and Robson, S.: Straightforward reconstruction of 3D surfaces and
651 topography with a camera: accuracy and geoscience application. *Journal of
652 Geophysical Research*, 117, F03017, doi: 10.1029/2011JF002289, 2012.

653

654 James, M. R. and Robson, S.: Mitigating systematic error in topographic models
655 derived from UAV and ground-based image networks. *Earth Surface Processes and*
656 *Landforms*, 39, 1413-1420, doi: 10.1002/esp.3609, 2014.

657
658 James, M. R., Robson, S., Pinkerton, H., and Ball, M.: Oblique photogrammetry with
659 visible and thermal images of active lava flows. *Bulletin of Volcanology*, 69, 105-108,
660 doi: 10.1007/200445-006-0062-9, 2006.

661
662 Javernick, L., Brasington, J., and Caruso, B.: Modelling the topography of shallow
663 braided rivers using Structure-from-Motion photogrammetry. *Geomorphology*, 213,
664 116-182, doi: 10.1016/j.geomorph.2014.01.006, 2014.

665
666 Kääh, A.: Monitoring high-mountain terrain deformation from repeated air- and
667 spaceborne optical data: examples using digital aerial imagery and ASTER data.
668 *ISPRS Journal of Photogrammetry and Remote Sensing*, 57(1-2), 39-52, doi:
669 10.1016/S0924-2716(02)00114-4, 2002.

670
671 Kääh, A., Girod, L., and Berthling, L.: Surface kinematics of periglacial sorted circles
672 using structure-from-motion technology. *The Cryosphere*, 8, 1041-1056, doi:
673 10.5194/tc-8-1041-2014, 2014.

674
675 Keim, R. F., Skaugset, A. E., and Bateman, D. S.: Digital terrain modelling of small
676 stream channels with a total-station theodolite. *Advances in Water Resources*, 23,
677 41-48, doi: 10.1016/S0309-1708(99)00007-X, 1999.

678
679 Keutterling, A. and Thomas, A.: Monitoring glacier elevation and volume changes
680 with digital photogrammetry and GIS at Gepatschferner glacier, Austria. *International*
681 *Journal of Remote Sensing*, 27(19), 4371-4380, doi: 10.1080/01431160600851819,
682 2006.

683
684 Kraaijenbrink, P., Meijer, S. W., Shea, J. M., Pellicciotti, F., de Jong, S. M., and
685 Immerzeel W. W.: Seasonal surface velocities of a Himalayan glacier derived by
686 automated correlation of unmanned aerial vehicle imagery. *Annals of Glaciology*,
687 57(71), 103-113, doi: 10.3189/2016AoG71A072, 2016.

688
689 [Krüger, J., and Kjær, K.H.: De-icing progression of ice-cored moraines in a humid,](#)
690 [subpolar climate, Kötlujökull, Iceland. *The Holocene*, 10\(6\), 737-747, doi:](#)
691 [10.1191/09596830094980, 2000.](#)

692
693 Lague, D., Brodu, N., and Leroux, J.: Accurate 3D comparison of complex
694 topography with terrestrial laser scanner: Application to the Rangitikei canyon (N-Z).
695 *ISPRS Journal of Photogrammetry and Remote Sensing*, 82, 10-26, doi:
696 10.1016/j.isprsjprs.2013.04.009, 2013.

697
698 Lewis, A., Hilley, G. E., and Lewicki, J. L.: Integrated thermal infrared imaging and
699 structure-from-motion photogrammetry to map apparent temperature and radiant
700 hydrothermal heat flux at Mammoth Mountain, CA, USA. *Journal of Volcanology and*
701 *Geothermal Research*, 303, 16-24, doi: 10.1016/j.jvolgeores.2015.07.025, 2015.

702

Formatted: Font: 12 pt, Not Bold

703 Lowe, D. G.: Distinctive image features from scale-invariant keypoints. *International*
704 *Journal of Computer Vision*, 60(2), 91-110, doi:
705 10.1023/B%VISI.0000029664.99615.94, 2004.
706

707 Micheletti, N., Chandler, J. H., and Lane, S. N.: Investigating the geomorphological
708 potential of freely available and accessible structure-from-motion photogrammetry
709 using a smartphone. *Earth Surface Processes and Landforms*, 40(4), 473-486, doi:
710 10.1002/esp.3648, 2014.
711

712 Micheletti, N., Lane, S. N., and Chandler, J. H.: Application of archival aerial
713 photogrammetry to quantify climate forcing of Alpine landscapes. *The*
714 *Photogrammetric Record*, 30(150), 143-165, doi: 10.1111/phor.12099, 2015.
715

716 Milan, D. J., Heritage, G. L., and Hetherington, D.: Application of a 3D laser scanner
717 in the assessment of erosion and deposition volumes and channel change in a
718 proglacial river. *Earth Surface Processes and Landforms*, 32, 1657-1674, doi:
719 10.1002/esp.1592, 2007.
720

721 Niethammer, U., Rothmund, S., James, M. R., Traveletti, J., and Joswig, M.: UAV-
722 based remote sensing of landslide. *International Archives of the Photogrammetry,*
723 *Remote Sensing and Spatial Information Sciences*, 38(5), 496-501, doi:
724 10.1016/j.enggeo.2011.03.012, 2010.
725

726 Noh, M-J. and Howat, I. M.: Automated stereo-photogrammetric DEM generation at
727 high latitudes: Surface Extraction with TIN-based Search-space Minimization
728 (SETSM) validation and demonstration over glaciated regions. *GIScience and*
729 *Remote Sensing*, 52(2), doi: 10.1080/15481603.2015.1008621, 198-217, 2015.
730

731 Ouédraogo, M. M., Degré, A., Debouche, C., and Lisein, J.: The evaluation of
732 unmanned aerial system-based photogrammetry and terrestrial laser scanning to
733 generate DEMs of agricultural watersheds. *Geomorphology*, 214, 339-355, doi:
734 10.1016/j.geomorph.2014.02.016, 2014.
735

736 Passalacqua, P., Hillier, J., and Tarolli, P.: Innovative analysis and use of high-
737 resolution DTMs for quantitative interrogation of Earth-surface processes. *Earth*
738 *Surface Processes and Landforms*, 39, 1400-1403, doi: 10.1002/esp.3616, 2014.
739

740 Passalacqua, P., Belmont, P., Staley, D. M., Simley, J. D., Arrowsmith, J. R., Bode,
741 C. A., Crosby, C., DeLong, S. B., Glenn, N. F., Kelly, S. A., Lague, D., Sangireddy,
742 H., Schaffrath, K., Tarboton, D. G., Waskiewicz, T., and Wheaton, J. M.: Analyzing
743 high resolution topography for advancing the understanding of mass and energy
744 transfer through landscapes: A review. *Earth-Science Reviews*, 148, 174-193, doi:
745 10.1016/j.earscirev.2015.05.012, 2015.
746

747 Pepin, N. C., Duane, W. J., Schaefer, M., Pike, G., and Hardy, D. R.: Measuring and
748 modeling the retreat of the summit ice fields on Kilimanjaro, East Africa. *Arctic,*
749 *Antarctic and Alpine Research*, 46(4), 905-917, doi: 10.1657/1938-4246-46.4.905,
750 2014.
751

752 Piermattei, L., Carturan, L., and Guarnieri, A.: Use of terrestrial photogrammetry
753 based on structure-from-motion for mass balance estimation of a small glacier in the
754 Italian alps. *Earth Surface Processes and Landforms*, 40, 1791-1802, doi:
755 10.1002/esp.3756, 2015.

756

757 Pitkänen, T. and Kajuutti, K.: Close-range photogrammetry as a tool in glacier
758 change detection. *International Archives of the Photogrammetry, Remote Sensing*
759 *and Spatial Information Sciences (ISPRS)*, 35, 769-773, 2004.

760

761 Reid, T. D., Carenzo, M., Pellicciotti, F., and Brock, B. W.: Including debris cover
762 effects in a distributed model of glacier ablation. *Journal of Geophysical Research:*
763 *Atmospheres*, 117, D18105, doi: 10.1029/2012JD017795, 2012.

764

765 Rippin, D. M., Pomfret, A., and King, N.: High resolution mapping of supra-glacial
766 drainage pathways reveals links between micro-channel drainage density, surface
767 roughness and surface reflectance. *Earth Surface Processes and Landforms*,
768 40(10), 1279-1290, doi: 10.1002/esp.3719, 2015.

769

770 Rosnell, T. and Honkavaara, E.: Point cloud generation from aerial image data
771 acquired by a quadcopter type micro unmanned aerial vehicle and a digital still
772 camera. *Sensors*, 12, 453-480, doi: 10.3390/s120100453, 2012.

773

774 Rosser, N. J., Petley, D. N., Lim, M., Dunning, S. A., and Allison, R. J.: Terrestrial
775 laser scanning for monitoring the process of hard rock coastal cliff erosion. *Quarterly*
776 *Journal of Engineering Geology & Hydrogeology*, 38, 363-375, 2005.

777

778 Ryan, J. C., Hubbard, A. L., Box, J. E., Todd, J., Christoffersen, P., Carr, J. R., Holt,
779 T. O., and Snooke, N.: UAV photogrammetry and structure from motion to assess
780 calving dynamics at Store Glacier, a large outlet draining the Greenland ice sheet.
781 *The Cryosphere*, 9, 1-11, doi: 10.5194/tc-9-1-2015, 2015.

782

783 Sanz-Ablanedo, E., Chandler, J. H., and Irvine-Fynn, T. D. L.: Studying glacial melt
784 processes using sub-centimeter DEM extraction and digital close-range
785 photogrammetry. *ISPRS Archives*, 39(B5), 435-440, 2012.

786

787 [Schomacker, A.: What controls dead-ice melting under different climate conditions?](#)
788 [A discussion. Earth-Science Reviews, 90, 103-113, doi:](#)
789 [10.1016/j.earscirev.2008.08.003, 2008.](#)

790

791 Schwalbe, E. and Maas, H. G.: Motion analysis of fast flowing glaciers from multi-
792 temporal terrestrial laser scanning. *Photogrammetrie Fernerkundung*
793 *Geoinformation*, 1, 91-98, doi: 10.1127/0935-1221/2009/0009, 2009.

794

795 Sinisalo, A. and Moore, J. C.: Antarctic blue ice area – towards extracting
796 paleoclimate information. *Antarctic Science*, 22(2), 99-115, doi:
797 10.107/S0954102009990691, 2010.

798

799 Smith, M. J., Rose, J., and Booth, S.: Geomorphological mapping of glacial
800 landforms from remotely sensed data: An evaluation of the principal data sources

801 and an assessment of their quality. *Geomorphology*, 76(1-2), 148-165, doi:
802 10.1016/j.geomorph.2005.11.001, 2006.
803
804 Smith, M. J., Rose, J., and Gousie, M. B.: The Cookie Cutter: A method for obtaining
805 a quantitative 3D description of glacial bedforms. *Geomorphology*, 108, 209-218, doi:
806 10.1016/j.geomorph.2009.01.006, 2009.
807
808 Smith, M. W. and Vericat, D.: From experimental plots to experiment landscapes:
809 topography, erosion and deposition in sub-humid badlands from Structure-from-
810 Motion photogrammetry. *Earth Surface Processes and Landforms*, doi:
811 10.1002/esp.3747, 2015.
812
813 Spaulding, N. E., Spikes, V. B., Hamilton, G. S., Mayewski, P. A., Dunbar, N. W.,
814 Harvey, R. P., Schutt, J., and Kurbatov, A. V.: Ice motion and mass balance at the
815 Allan Hills blue-ice area, Antarctica, with implications for paleoclimate
816 reconstructions. *Journal of Glaciology*, 58(208), 399-406, doi:
817 10.3189/2012JoG11J176, 2012.
818
819 Staines, K. E. H., Carrivick, J. L., Tweed, F. S., Evans, A. J., Russell, A. J.,
820 Jóhannesson, T., and Roberts, M.: A multi-dimensional analysis of pro-glacial
821 landscape change at Sólheimajökull, southern Iceland. *Earth Surface Processes and*
822 *Landforms*, 40, 809-822, doi: 10.1002/esp.3662, 2015.
823
824 Stumpf, A., Malet, J-P., Allemand, P., and Ulrich, P.: Surface reconstruction and
825 landslide displacement measurements with Pléiades satellite images. *ISPRS Journal*
826 *of Photogrammetry and Remote Sensing*, 95, 1-12, doi:
827 10.1016/j.isprsjprs.2014.05.008, 2014.
828
829 Tarolli, P.: High-resolution topography for understanding Earth surface processes:
830 Opportunities and challenges. *Geomorphology*, 216, 295-312, doi:
831 10.1016/j.geomorph.2014.03.008, 2014.
832
833 Tonkin, T. N., Midgley, N. G., Graham, D. J., and Labadz, J. C.: The potential of
834 small unmanned aircraft systems and structure-from-motion for topographic surveys:
835 a test of emerging integrated approaches at Cwm Idwal, North Wales.
836 *Geomorphology*, 226, 35-43, doi: 10.1016/j.geomorph.2014.07.021, 2014.
837
838 Vieira, R., Hinata, S., da Rosa, K. K., Zilberstein, S., and Simoes, J. C.: Periglacial
839 features in Patriot Hills, Ellsworth Mountains, Antarctica. *Geomorphology*, 155-156,
840 96-101, doi: 10.1016/j.geomorph.2011.12.014, 2012.
841
842 Westoby, M. J., Brasington, J., Glasser, N. F., Hambrey, M. J., and Reynolds, J. M.:
843 'Structure-from-Motion' photogrammetry: A low-cost, effective tool for geoscience
844 applications. *Geomorphology*, 179, 300-314, doi: 10.1016/j.geomorph.2012.08.021,
845 2012.
846
847 Westoby, M. J., Dunning, S. A., Woodward, J., Hein, A. S., Marrero, S. M., Winter,
848 K., and Sugden, D. E.: Sedimentological characterisation of Antarctic moraines
849 using UAVs and Structure-from-Motion photogrammetry. *Journal of Glaciology*, ~~in~~
850 [press 61\(230\), 1088-1102, doi: 10.3189/2015JoG15J086, 2015.](https://doi.org/10.3189/2015JoG15J086)

851
852 Wheaton, J. M., Brasington, J., Darby, S. E., and Sear, D. A.: Accounting for
853 uncertainty in DEMs from repeat topographic surveys: improved sediment budgets.
854 *Earth Surface Processes and Landforms*, 35, 136-156, doi: 10.1002/esp.1886, 2010.
855
856 Whitehead, K., Moorman, B., and Wainstein, P.: Measuring daily surface elevation
857 and velocity variations across a polythermal arctic glacier using ground-based
858 photogrammetry. *Journal of Glaciology*, 60(224), 1208-1220, doi:
859 10.3189/2014JoG14J080, 2014.
860
861 Woodget, A. S., Carbonneau, P. E., Visser, F., and Maddock, I. P.: Quantifying
862 submerged fluvial topography using hyperspatial resolution UAS imagery and
863 structure from motion photogrammetry. *Earth Surface Processes and Landforms*,
864 40(1), 47-64, doi: 10.1002/esp.3613, 2015.
865

866 **Table 1**

Field survey	Scan position	Scan date	Scan-scan registration error (RMS; m)	Project-project registration error (RMS; m)
Season 1 start (TLS)	1	07 Dec 2012	Static	Static
	2	08 Dec 2012	0.0327	
	3	08 Dec 2012	0.0391	
	5	09 Dec 2012	0.0301	
	6	01 Dec 2012	0.0258	
	7	11 Dec 2012	0.0258	
Season 1 end (TLS)	1	09 Jan 2013	Static	0.0145
	2	09 Jan 2013	0.0145	
Season 1 end (UAV-SfM)	-	05 Jan 2013	-	0.0306
Season 2 (TLS)	1	14 Jan 2014	Static	0.0149
	2	14 Jan 2014	0.0205	
	3	14 Jan 2014	0.0255	

867 **Table 2**
868

Differencing epoch	Propagated error (RMS; m)	M3C2 $LoD_{95\%}$ (m)
S1 start (TLS) - S1 end (TLS)	0.049	0.098
S1 start (TLS) - S1 end (SfM)	0.050	0.103
S1 end (TLS) - S2 end (TLS)	0.048	0.098
S1 end (SfM) - S2 end (TLS)	0.049	0.102
S1 start (TLS) - S2 end (TLS)	0.050	0.099

869 **Figure captions**

Formatted: Font: Bold

870
871 **Figure 1.** Blue-ice moraine embayment, Patriot Hills, Heritage Range, Antarctica. **(a)**
872 Geographical context of Patriot Hills within the Heritage Range, southern Ellsworth
873 Mountains. Antarctica context map. Red star is location of the Heritage Range. Black
874 dot indicates location of the geographic south pole. **(b)** The Patriot Hills massif. The
875 location of the study embayment and area displayed in **(c)** is highlighted in red. **(c)**:
876 Detailed study site overview map. Contours and underlying hillshade are derived
877 from a UAV-SfM-derived DEM. TLS scanning positions for the start of season 1 are
878 shown in red, blue and yellow. The two scan positions re-occupied at the end of
879 season 1 are shown in blue, whilst the three scan positions reoccupied in season 2
880 are shown in blue and red. Background to **(ba)** is © U.S. Geological Survey, **(b)** 2015
881 DigitalGlobe, both extracted from Google Earth (imagery date: 03/10/2009).

Formatted: Font: Bold

882
883 **Figure 2.** Field photographs of the Patriot Hills blue-ice moraine study site. **(a)**
884 Panoramic photograph of the moraine embayment – view north-east towards the ice
885 margin from the rear of the embayment. Area shown in **(c)** and position and view
886 direction of camera **(b)** shown for reference. **(b)** View to the north-west with moraine
887 crest in foreground and subdued, ice-marginal moraine surface topography in
888 middle-ground. **(c)** Close-up of moraine topography, highlighting ridges and furrows
889 on moraine crests and in inter-moraine troughs.

890
891 **Figure 3.** Results of vertical (Z_{diff} ; m) differencing of the UAV-SfM and TLS datasets
892 acquired at the end of season 1, represented as the mean difference within 10 m²
893 grid cells. 83% of the UAV-SfM data were found to be within ±0.1 m of the equivalent
894 TLS data. Profiles A-C are displayed in Fig. 4.

895
896 ~~**Figure 3.** Vertical component of 3D topographic change (Z_{diff}) overlain on a UAV-~~
897 ~~SfM-derived hill shaded DEM of the Patriot Hills blue ice moraine complex.~~
898 ~~Topographic evolution was quantified using the Multiscale Model to Model Cloud~~
899 ~~Comparison (M3C2) algorithm in CloudCompare software. **(a)** UAV-SfM~~
900 ~~orthophotograph of the study site. Panels **(b)** to **(f)** cover specific differencing epochs~~
901 ~~using a combination of TLS and SfM data (see panel headings). Dashed line in **(b)** to~~
902 ~~**(f)** indicates locations of primary moraine ridge crest.~~

903
904 **Figure 45.** Moraine surface elevation profiles, extracted from gridded (0.2 m²) digital
905 elevation models of TLS- and SfM-derived topographic datasets. Profile locations are
906 shown in Figures 43 and 6. Profiles A and B bisect the main central moraine crest,
907 whilst profile C is located on moraine deposits at the back of the embayment. Inset
908 numbered boxes in profiles A and C show areas referred to in the text.

909
910 **Figure 35.** Vertical component of 3D topographic change (Z_{diff}) overlain on a UAV-
911 SfM-derived hill-shaded DEM of the Patriot Hills blue-ice moraine complex.
912 Topographic evolution was quantified using the Multiscale Model to Model Cloud

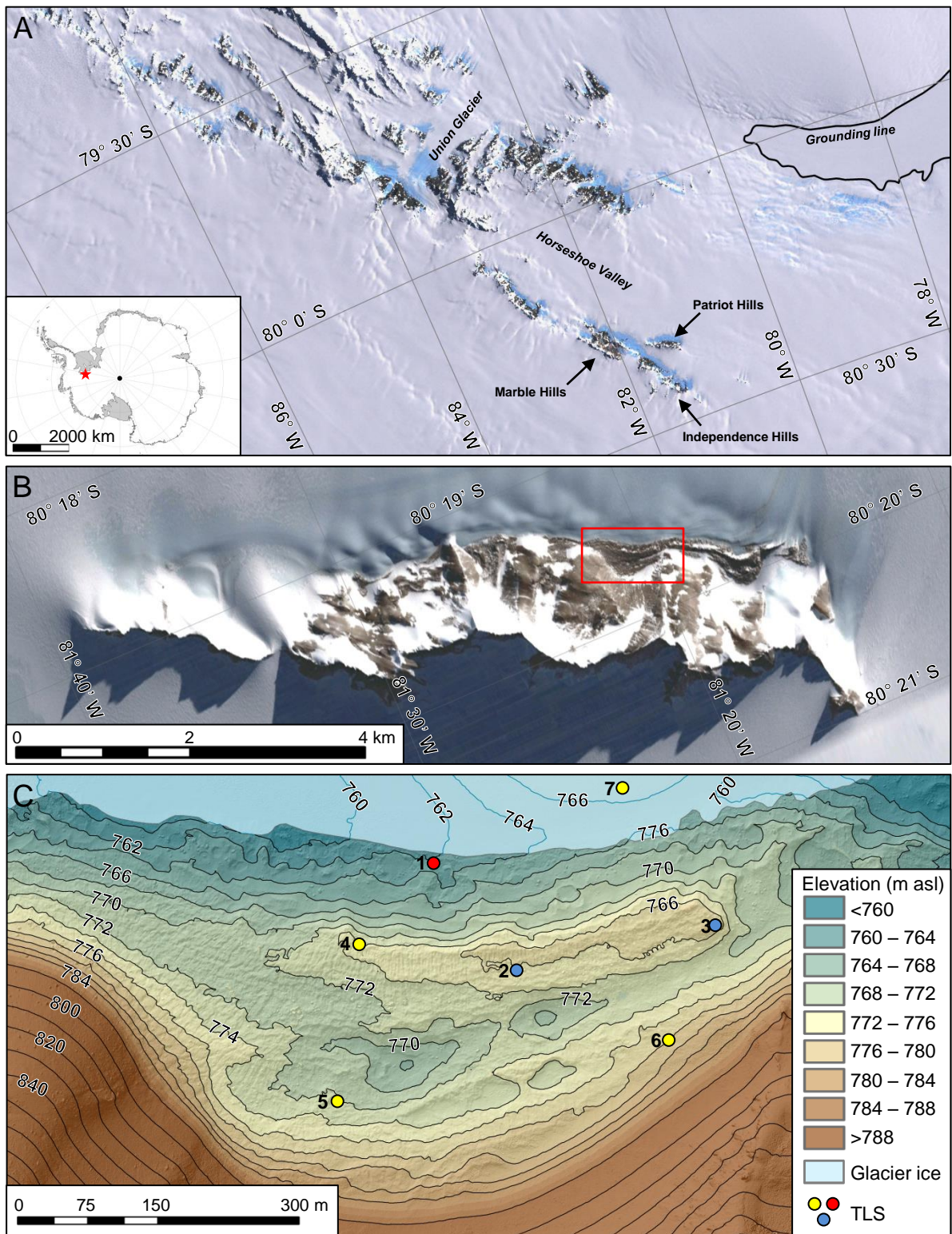
913 Comparison (M3C2) algorithm in CloudCompare software. (a) UAV-SfM
914 orthophotograph of the study site. Panels (b) to (f) cover specific differencing epochs
915 using a combination of TLS and SfM data (see panel headings). Dashed line in (b) to
916 (f) indicates locations of primary moraine ridge crest.
917
918

919 **Figure 46.** Change detection mapping for (a) intra-annual (season 1 start to season
920 1 end) and (b) annual (season 1 start to season 2) differencing epochs. Horizontal
921 difference vectors (XY_{diff}) are scaled by magnitude and oriented according to the
922 direction of change. The vertical component of 3D change (Z_{diff}) is shown in the
923 background. Transects A-C denote the location of moraine surface profiles displayed
924 in Fig. 45. Red dashes on both panels show approximate location of primary moraine
925 ridge crest.
926

927 ~~Figure 5. Moraine surface elevation profiles, extracted from gridded (0.2 m^2) digital~~
928 ~~elevation models of TLS and SfM derived topographic datasets. Profile locations are~~
929 ~~shown in Fig. 4. Profiles A and B bisect the main central moraine crest, whilst profile~~
930 ~~C is located on moraine deposits at the back of the embayment. Inset numbered~~
931 ~~boxes in profiles A and C show areas referred to in the text.~~
932

933 **Table 1.** Terrestrial laser scanning and UAV-SfM survey dates and registration
934 errors. Within each season, individual scans were registered to a single static
935 position to produce a single, merged point cloud (scan-scan registration error). TLS
936 data from the end of season 1 and for season 2 were subsequently registered to TLS
937 data acquired at the start of season 1, producing a project-project registration error.
938 The UAV-SfM data (season 1 end) were registered to TLS data from the end of
939 season 1.
940

941 **Table 2.** Registration error propagation for specific differencing epochs. The
942 propagated error for each differencing epoch is calculated using Eq. 3. The 95%
943 level of detection, or detection threshold is calculated in M3C2 as the product of the
944 propagated error and a measure of local point cloud roughness (Lague et al., 2013).
945 The results of 3D differencing were filtered in CloudCompare so that only differences
946 largest than the most conservative (largest) $LoD_{95\%}$ (i.e. 0.103 m) were considered to
947 represent significant change.
948



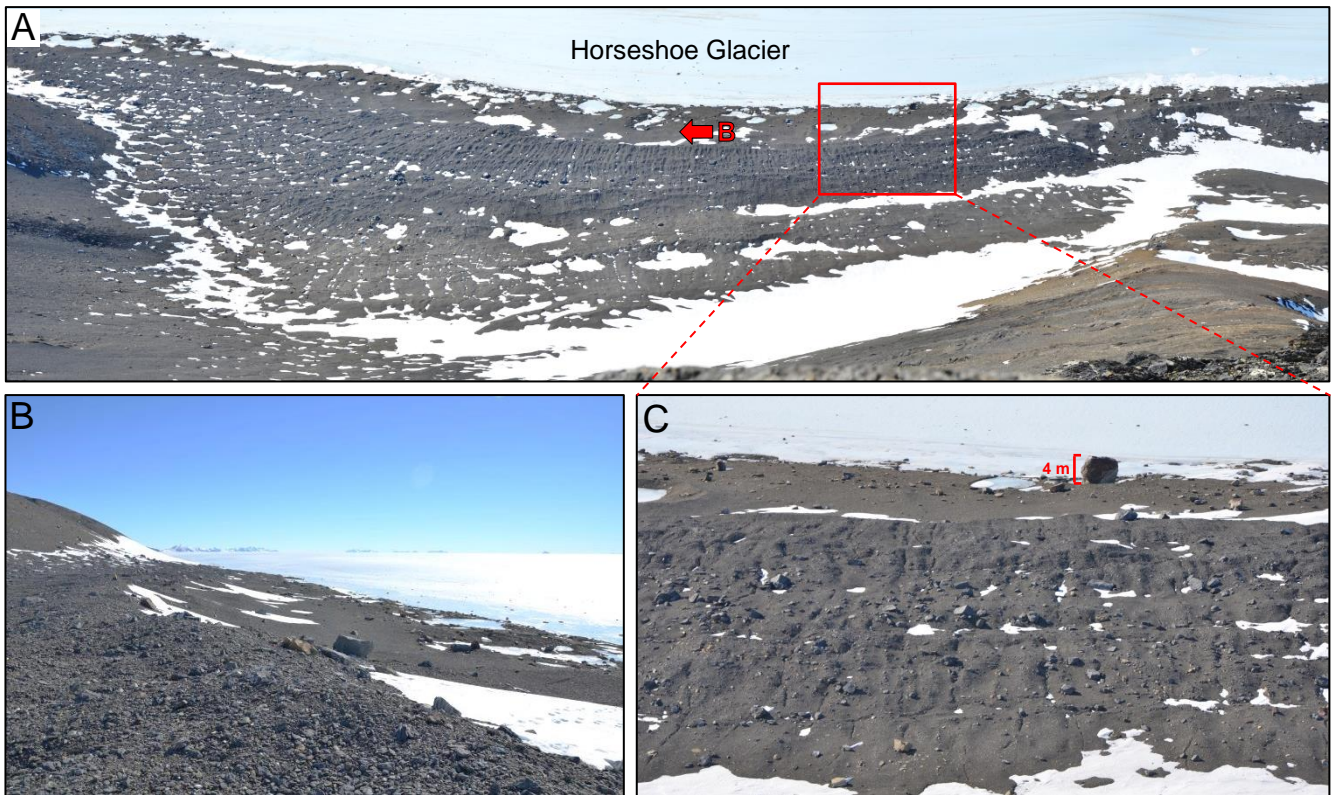


Figure 2. Field photographs of the Patriot Hills blue-ice moraine study site. **(a)** Panoramic photograph of the moraine embayment – view north-east towards the ice margin from the rear of the embayment. Area shown in **(c)** and position and view direction of camera **(b)** shown for reference. **(b)** View to the north-west with moraine crest in foreground and subdued, ice-marginal moraine surface topography in middle-ground. **(c)** Close-up of moraine topography, highlighting ridges and furrows on moraine crests and in inter-moraine troughs.

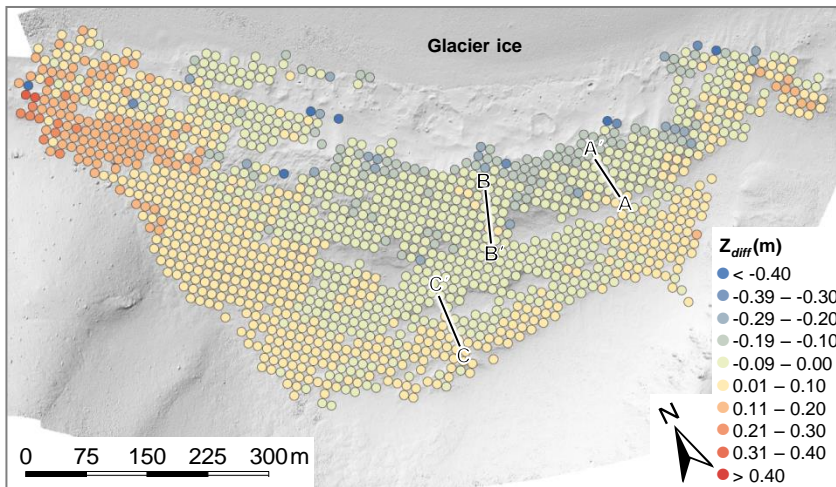


Figure 3. Results of vertical (Z_{diff} ; m) differencing of the UAV-SfM and TLS datasets acquired at the end of season 1, represented as the average difference within 10 m² grid cells. 83% of the UAV-SfM data were found to be within ± 0.1 m of the equivalent TLS data. Profiles A-C are displayed in Fig. 4.

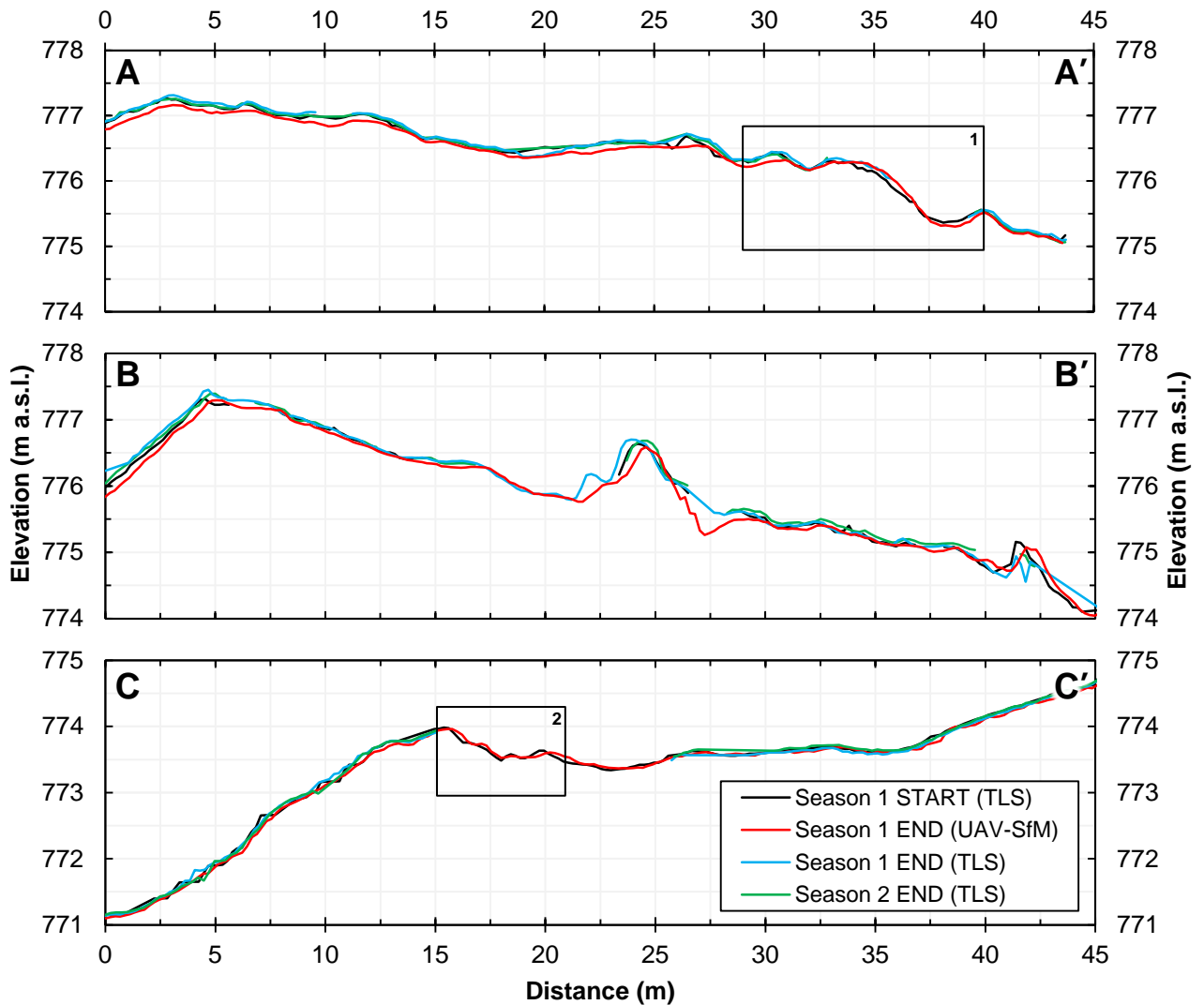


Figure 4. Moraine surface elevation profiles, extracted from gridded (0.2 m^2) digital elevation models of TLS- and SfM-derived topographic datasets. Profile locations are shown in Fig. 4. Profiles A and B bisect the main central moraine crest, whilst profile C is located on moraine deposits at the back of the embayment. Inset numbered boxes in profiles A and C show areas referred to in the text.

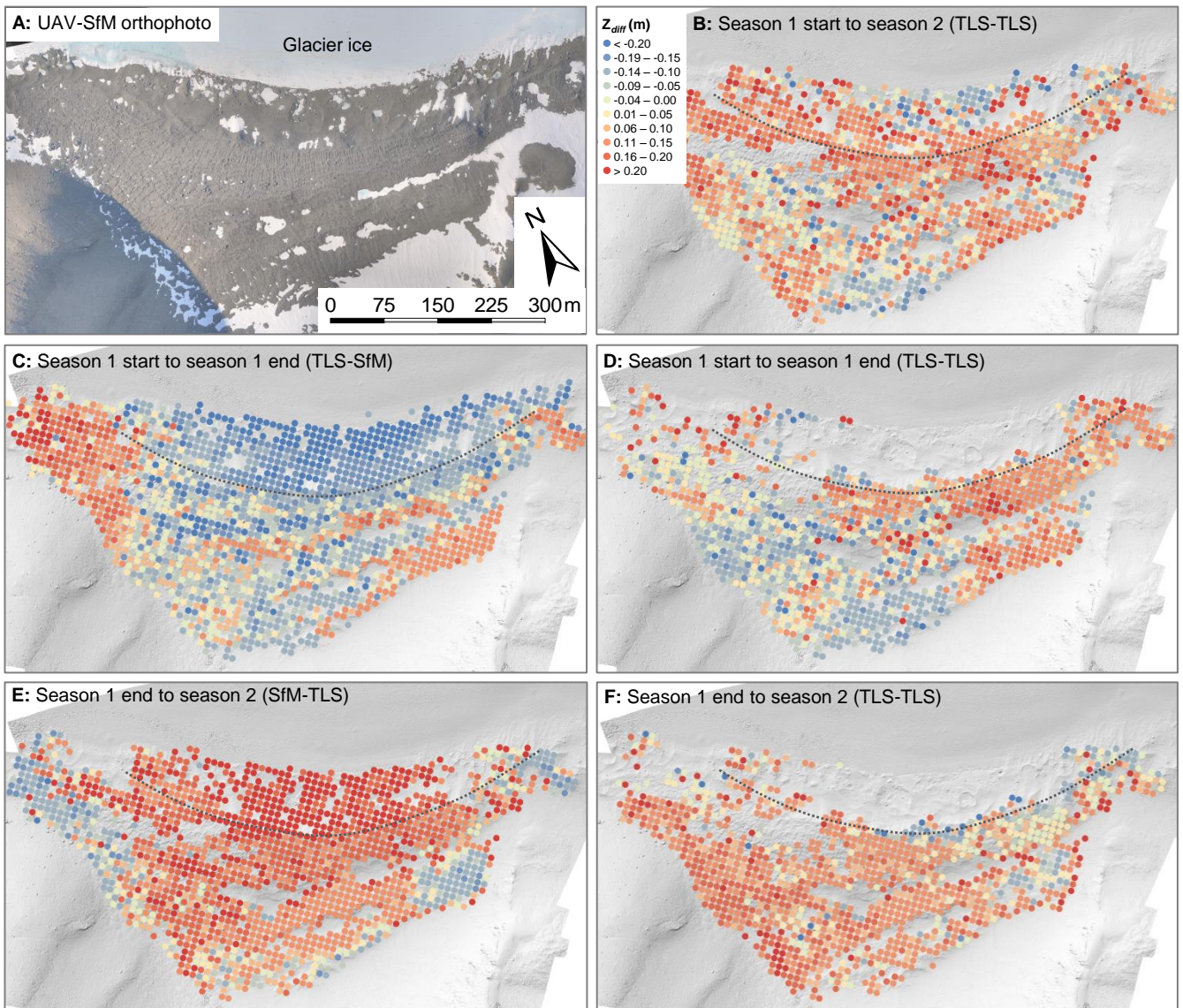


Figure 5. Vertical component of 3D topographic change (Z_{diff}) overlain on a UAV-SfM-derived hill-shaded DEM of the Patriot Hills blue-ice moraine complex. Topographic evolution was quantified using the Multiscale Model to Model Cloud Comparison (M3C2) algorithm in CloudCompare software. **(a)** UAV-SfM orthophoto of the study site. Panels **(b)** to **(f)** cover specific differencing epochs using a combination of TLS and SfM data (see panel headings). Dashed line in **(b)** to **(f)** indicates locations of primary moraine ridge crest.

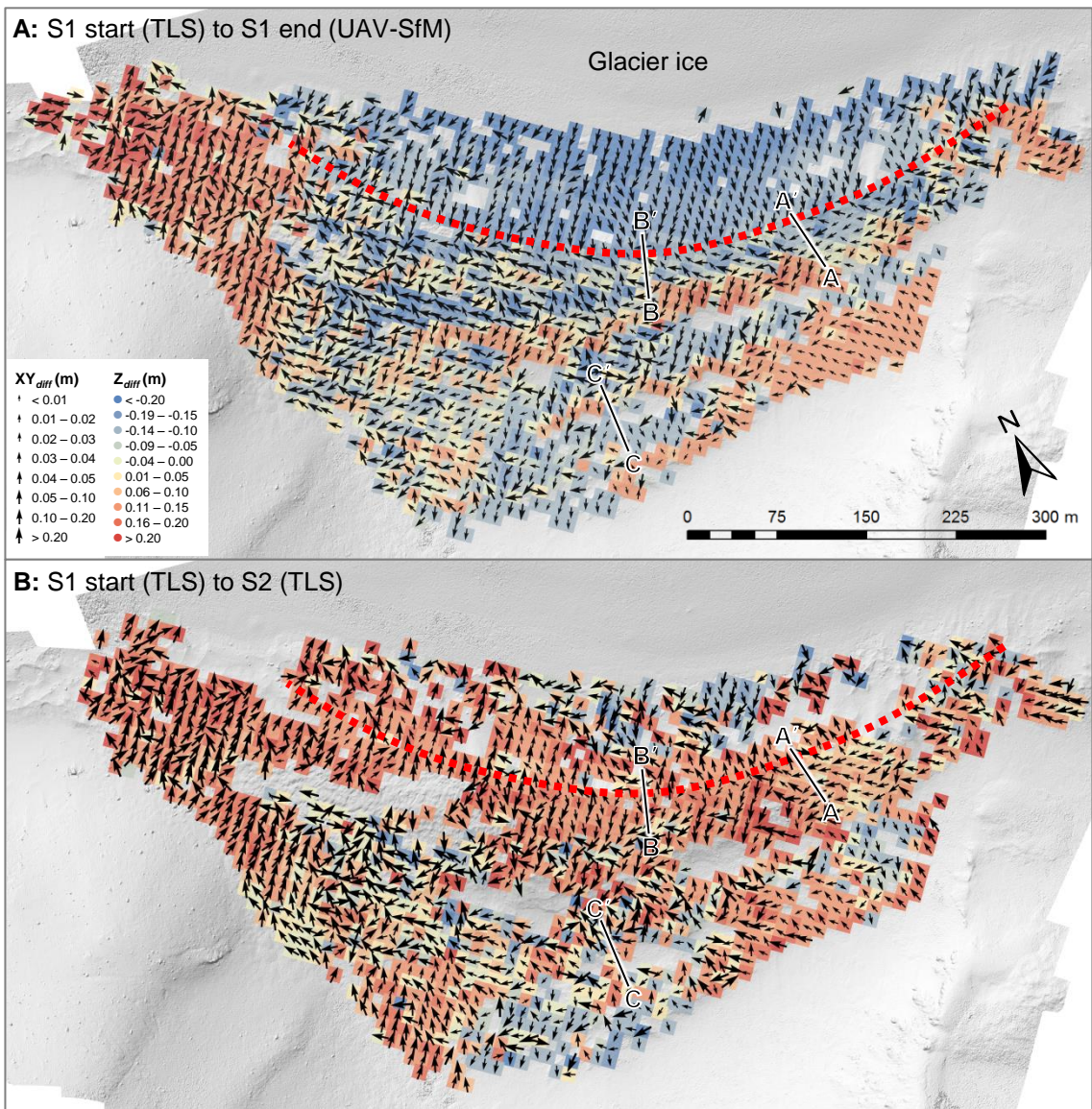


Figure 6. Change detection mapping for **(a)** intra-annual (season 1 start to season 1 end) and **(b)** annual (season 1 start to season 2) differencing epochs. Horizontal difference vectors (XY_{diff}) are scaled by magnitude and oriented according to the direction of change. The vertical component of 3D change (Z_{diff}) is shown in the background. Transects A-C denote the location of moraine surface profiles displayed in Fig. 5. Red dashes on both panels show approximate location of primary moraine ridge crest.

Table 1. Terrestrial laser scanning and UAV-SfM survey dates and registration errors. Within each season, individual scans were registered to a single static position to produce a single, merged point cloud (scan-scan registration error). TLS data from the end of season 1 and for season 2 were subsequently registered to TLS data acquired at the start of season 1, producing a project-project registration error. The UAV-SfM data (season 1 end) were registered to TLS data from the end of season 1.

Field survey	Scan position	Scan date	Scan-scan registration error (RMS; m)	Project-project registration error (RMS; m)
Season 1 start (TLS)	1	07 Dec 2012	Static	Static
	2	08 Dec 2012	0.0327	
	3	08 Dec 2012	0.0391	
	5	09 Dec 2012	0.0301	
	6	01 Dec 2012	0.0258	
	7	11 Dec 2012	0.0258	
	Season 1 end (TLS)	1	09 Jan 2013	Static
2		09 Jan 2013	0.0145	
Season 1 end (UAV-SfM)	-	05 Jan 2013	-	0.0306
Season 2 (TLS)	1	14 Jan 2014	Static	0.0149
	2	14 Jan 2014	0.0205	
	3	14 Jan 2014	0.0255	

Table 2. Registration error propagation for specific differencing epochs. The propagated error for each differencing epoch is calculated using Eq. 3. The 95% level of detection, or detection threshold is calculated in M3C2 as the product of the propagated error and a measure of local point cloud roughness (Lague et al., 2013). The results of 3D differencing were filtered in CloudCompare so that only differences largest than the most conservative (largest) $LoD_{95\%}$ (i.e. 0.103 m) were considered to represent significant change.

Differencing epoch	Propagated error (RMS; m)	M3C2 $LoD_{95\%}$ (m)
S1 start (TLS) - S1 end (TLS)	0.049	0.098
S1 start (TLS) - S1 end (SfM)	0.050	0.103
S1 end (TLS) - S2 end (TLS)	0.048	0.098
S1 end (SfM) - S2 end (TLS)	0.049	0.102
S1 start (TLS) - S2 end (TLS)	0.050	0.099